

SCIENTIFIC REPORTS



OPEN

Dynamic refractive index distribution measurement of dynamic process by combining dual-channel simultaneous phase-shifting interferometry and total internal reflection

Yunfei Zhou¹, Haoren Zou¹, Liyun Zhong¹, Jiaosheng Li¹, Bingbo Li¹, Jindong Tian² & Xiaoxu Lu¹

We propose and demonstrate a novel method to measure dynamic refractive index distributions using a combination of total internal reflection (TIR) and dual-channel simultaneous phase-shifting interferometry (DCSPSI). First, a right-angle prism is introduced into the DCSPSI system, the reflection phase variation induced by TIR, which contains the refractive index information of tested sample, can be achieved by the spatial carrier-frequency phase-shifting algorithm from a pair of interferograms with the phase shifts of $\pi/2$ captured by DCSPSI system. Second, based on the relationship between the reflection phase variation and the refractive index, the 2D refractive index distribution can be calculated easily. Importantly, the proposed TIR-DCSPSI method will supply a useful tool for dynamic refractive index distribution measurement of dynamic process, such as the droplet evaporation, mutual solubilization and diffusion of different droplets, cell culture, colloid curing, etc.

Refractive index distribution measurement of dynamic process is an important content for studying physical changes such as evaporation of solution, mutual solubilization of different liquids, diffusion process, etc. Abbe refractometer suffered from the disability of dynamic measurement of 2D refractive index distribution, even though the measurement results of which are recognized as standards in measuring the refractive index of transparent and translucent liquid¹. Since the total internal reflection fluorescence microscopy was demonstrated in studying cell-substrate contact^{2,3}, studies on total internal reflection have been further developed in measuring kinds of optical parameters⁴⁻⁶. Methods based on total internal reflection to measure the refractive index of liquid have been proposed⁷⁻¹⁰. However, these methods fail to achieve dynamical measurement due to requirements of changing the angle of incident light or scanning that of reflected light to determine the critical angle, with which the refractive index is calculated. A method based on heterodyne interferometry is proposed^{11,12}. It needs to measure the reflection phase variation difference of s-polarization and p-polarization components of light when total internal reflection occurs. But it is incapable of measuring 2D refractive index distribution.

Phase-shifting interferometry (PSI)¹³ with the advantages of high accuracy, fast speed, full-field and nondestructive, has been extensively utilized in the phase measurement of transparent sample¹⁴⁻¹⁶. Recently, the digital holography based on total reflection technique has been proposed to achieve the refractive index distribution of homogeneous liquid¹⁷, its accuracy is affected by the filter window implemented at Fourier domain although it can achieve the dynamical measurement. Moreover, the PSI method based on total internal reflection is proposed

¹Guangdong Provincial Key Laboratory of Nanophotonic Functional Materials and Devices, South China Normal University, Guangzhou, 510006, China. ²Shenzhen Key Laboratory of Micro-Nano Measuring and Imaging in Biomedical Optics, College of Optoelectronic Engineering, Shenzhen University, Shenzhen, 518060, China. Correspondence and requests for materials should be addressed to X.L. (email: xiaoxulu48@sina.com)

to achieve the refractive index distribution of the static sample, but it is fail for dynamic process due to the requirement of continuous phase-shifting procedure¹⁸.

The refractive index distribution of dynamic process can be achieved by phase measurement. Many spatial phase-shifting interferometry (SPSI) methods have been introduced into dynamic process measurement^{19–23}. Fourier transform method extracts phase information by filtering technique, so the accuracy of phase retrieval is closely associated with the filtering window¹⁹. In SPSI, by using polarization components to produce phase shifts of orthogonal polarization beams, three or four phase-shifting interferograms can be captured simultaneously by three or four CCD cameras or three or four areas on a single polarized CCD, so three or four-step phase-shifting algorithm is introduced to perform the phase retrieval^{21–23}. Though the SPSI method can effectively restrain the noise by multi-frame phase-shifting interferograms, the synchronization problem of multiple CCD cameras makes the system complex, and the corresponding synchronization error also reduces the accuracy. To solve those problems, a dual-channel simultaneous phase-shifting interferometry (DCSPSI) is proposed²⁴, in which a pair of interferograms with the spatial phase shift of $\pi/2$ is captured simultaneously at one-time single exposure, so the phase retrieval of dynamic process can be achieved with two-step phase-shifting algorithm. Using this method, the dynamic phase distribution during dynamic process can be implemented easily.

In this paper, by combining total internal reflection (TIR) technique and our homemade dual-channel simultaneous phase-shifting interferometry (DCSPSI) system, we proposed a novel TIR-DCSPSI method to achieve dynamic 2D refractive index distribution during dynamic process. Following, we will introduce the proposed method in detail.

Methods

Our previous research has demonstrated that the DCSPSI system is a good candidate for dynamic phase measurement²⁴. In the proposed setup, a pair of spatial carrier-frequency interferograms (SCFIs) with a phase shift δ between them can be captured simultaneously by CCD1 and CCD2, which can be respectively expressed as:

$$I_{01}(x, y) = A(x, y) + B(x, y)\cos[\varphi(x, y) + \omega_x x + \omega_y y] \quad (1)$$

$$I_{02}(x, y) = A(x, y) + B(x, y)\cos[\varphi(x, y) + \omega_x x + \omega_y y + \delta]. \quad (2)$$

where, x and y represent the coordinates of pixels in CCD plane ($1 \leq x \leq M, 1 \leq y \leq N$); M and N are the number of columns and rows in the interferogram, respectively; $A(x, y)$ and $B(x, y)$ denote the background intensity and the modulation amplitude of interferogram, respectively; ω_x and ω_y are the spatial carrier frequencies along x and y directions, respectively; δ denotes the phase shift between two interferograms; $\varphi(x, y)$ is the measured phase. Typically, $A(x, y)$, $B(x, y)$ and $\varphi(x, y)$ are assumed to be unchanged between adjacent pixels if the measured phase is changed smoothly²⁵. Thus, two phase-shifting sub-interferograms with size of $(N-1) \times (M-1)$ can be constructed from each SCFI, so we have that

$$I_1(x, y) = I_{01}(x, y) \approx A(x, y) + B(x, y)\cos[\Phi(x, y) + \delta_1], \quad (3)$$

$$I_2(x, y) = I_{01}(x+1, y) \approx A(x, y) + B(x, y)\cos[\Phi(x, y) + \delta_2], \quad (4)$$

$$I_3(x, y) = I_{02}(x, y) \approx A(x, y) + B(x, y)\cos[\Phi(x, y) + \delta_3], \quad (5)$$

$$I_4(x, y) = I_{02}(x+1, y) \approx A(x, y) + B(x, y)\cos[\Phi(x, y) + \delta_4]. \quad (6)$$

where $I_1(x, y)$ and $I_2(x, y)$ are constructed from $I_{01}(x, y)$ while $I_3(x, y)$ and $I_4(x, y)$ are constructed from $I_{02}(x, y)$; $\delta_1, \delta_2, \delta_3$ and δ_4 denote the phase shifts between consecutive sub-interferograms, corresponding to $0, \omega_x, \delta$ and $\delta + \omega_x$, respectively; $\Phi(x, y) = \varphi(x, y) + \omega_x x + \omega_y y$ represents the phase including carrier-frequency. The measured phase $\varphi(x, y)$ can be calculated by the spatial carrier-frequency phase-shifting algorithm from the sub-interferograms²⁵

$$\varphi(x, y) = \text{unwrap}[\Phi(x, y)] - (\omega_x x + \omega_y y). \quad (7)$$

in which the symbol “unwrap” denotes a function of phase unwrapping operation.

In Fig. 1, a laser beam is incident from a denser medium with refractive index n_1 into a less dense one (droplet) with refractive index of n_2 . The total internal reflection occurs when the laser beam reaches the “prism-droplet” interface with the incident angle θ_1 , which is greater than the critical angle $\theta_c = \arcsin(n_2/n_1)$. Thus, there is no propagating wave in less dense medium except the evanescent wave exists near the interface, whose amplitude decays exponentially over a distance of a wavelength fraction. And all the light waves are reflected to the denser medium²⁶. As a result, the reflected wave produces a certain phase variation due to the Goos-Hanchen shift at the boundary²⁷, and the value of reflection phase variation depends on the indices of two-boundary and the incident angle. According to Fresnel formula²⁶, the reflection coefficients become complex

$$r_s = |r_s| \exp(i\psi_s), \quad \psi_s = -2 \arctan \frac{\sqrt{n_1^2 \sin^2 \theta_1 - n_2^2}}{n_1 \cos \theta_1}, \quad (8)$$

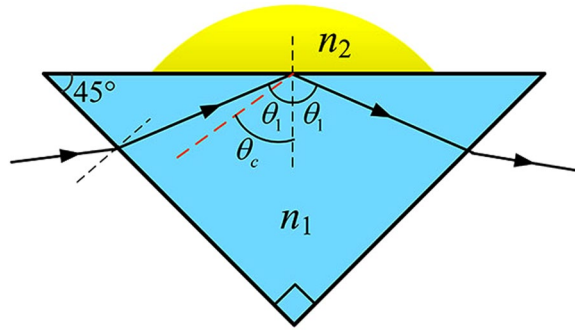


Figure 1. Schematic of total internal reflection at the boundary between the prism and tested droplet, in which n_1 and n_2 denote the refractive index of prism and droplet, respectively; θ_1 and θ_2 are the incident angle and critical angle, respectively.

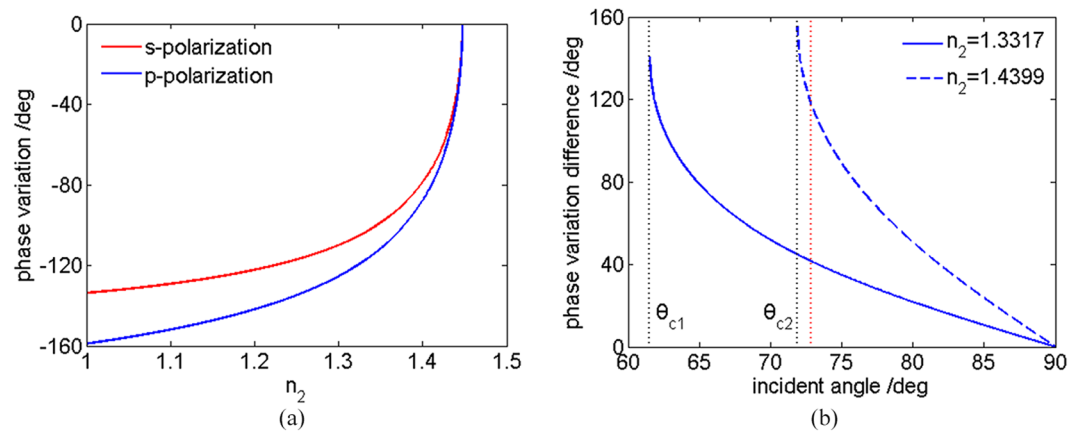


Figure 2. (a) The reflection phase variations ψ_s (s-polarization) and ψ_p (p-polarization) versus the refractive index n_2 in the case that incident angle $\theta_1 = 72.8^\circ$; (b) the reflection phase variation differences $\Delta\psi_{pt}$ (p-polarization) of different tested samples versus the incident angle θ_1 , in which the blue solid line and dashed line correspond to the water with n_2 of 1.3317 and the 80% glycerol-water with n_2 of 1.4399, respectively; the black dotted line on the left and on the right correspond to the critical angle $\theta_{c1} = 61.3^\circ$ with $n_2 = 1.3317$ and $\theta_{c2} = 71.9^\circ$ with $n_2 = 1.4399$, respectively; the red dotted line corresponds to the $\theta_1 = 72.8^\circ$ in the case that the prism refractive index $n_1 = 1.5151$ and air refractive index $n_0 = 1.0003$.

$$r_p = |r_p| \exp(i\psi_p), \quad \psi_p = -2 \arctan \frac{n_1 \sqrt{n_1^2 \sin^2 \theta_1 - n_2^2}}{n_2^2 \cos \theta_1} \tag{9}$$

where r_s and r_p denote the reflection coefficients of s-polarization and p-polarization; $|r_s|$ and $|r_p|$ are the modulus of reflection coefficients; ψ_s and ψ_p represents the reflection phase variations of s-polarization and p-polarization, respectively. Figure 2(a) illustrates the change of reflection phase variations ψ_s and ψ_p as function of the refractive index of n_2 . If $n_1 = 1.5151$ and $\theta_1 = 72.8^\circ$, the total internal reflection occurs, while $n_2 > 1.4775$ the total internal reflection disappears. For both s-polarization and p-polarization, the reflection phase variations are monotonically increasing with the refractive index n_2 , indicating the feasibility of refractive index measurement. In general, the reflection phase variation of p-polarization is larger than that of s-polarization for the same tested refractive index n_2 . Therefore, we choose the p-polarization as the object wave to improve the measuring sensitivity.

The configuration of the proposed TIR-DCSPSI system is illustrated in Fig. 3. A right-angle prism is introduced into the object arm of Mach-Zehnder interferometer. For convenience, the z-axis is placed along the laser propagation direction, the x-axis and y-axis are parallel and perpendicular to the paper plane, as the three-dimensional coordinates shown in the center, respectively. The tested sample is placed on the center of the hypotenuse prism surface, as the top view of the prism shown in the dashed box “A”. First, a frequency stabilized He-Ne laser with wavelength of 632.8 nm (Melles Griot, 05STP912) is utilized as the light source, and the intensity and polarization direction of laser beam can be adjusted by a variable neutral density filter (ND) and a half wave plate (HWP), respectively. Second, the laser beam is divided into two orthogonal polarization beams by the polarized beam splitter (PBS) after expanded and collimated by beam expander (BE), in which the transmitted beam with the parallel polarization direction to x-axis is utilized as the reference beam, and the reflected beam with the parallel polarization direction to y-axis is utilized as the object beam, in which the refractive index of right-angle

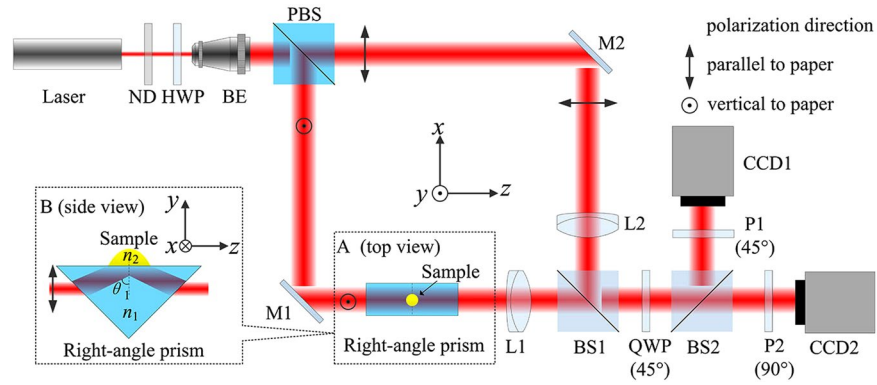


Figure 3. The configuration of the proposed TIR-DCSPSI system. ND, variable neutral density filter; HWP, half wave plate; BE, beam expander; PBS, polarized beam splitter; M1,M2 mirror; L1, L2, lens; BS1, BS2, non-polarized beam splitter; QWP, quarter wave plate; P1, P2, polarizer. Dashed boxes A and B are the top and side view of right-angle prism respectively.

prism is 1.5151 (Schott BK7 glass). A high-resolution rotation stage (Newport, 9411-M) with an angular sensitivity of 0.0025° was used to mount and rotate the right-angle prism. As the side view of right-angle prism shown in the dashed box “B” on the left of Fig. 3, by adjusting the prism, if the incident and output beams become coaxial, and the incident angle θ_1 at the prism hypotenuse is equal to 72.8°, the total internal reflection occurs at both prism-air interface and prism-droplet interface, in which the object beam can be considered as a p-polarization beam, it is assumed that the air around the prism is uniform with refractive index n_0 of 1.0003 in the airtight experimental environment²⁸. Third, the reference beam and object beam arrive at the first non-polarized beam splitter (BS1), and then pass through the quarter wave plate (QWP) with the fast axis 45° to x-axis, so two orthogonal circular polarization beams can be achieved. After that, each circular polarization beam is divided into two parts by the second non-polarized beam splitter (BS2), and two orthogonal interferograms are formed on CCD1 and CCD2 after the beams transmit through the first polarizer (P1) and the second polarizer (P2), in which the polarization direction of P1 and P2 are respectively 45° and 90° to the x-axis, and a certain amount of spatial carrier frequency can be produced by a small angle tilt for the reference beam and object beam. The spatial carrier frequency should be on a diagonal with respect to the CCD plane to ensure that its component along x-axis or y-axis is not zero. Finally, a pair of interferograms with the spatial phase shifts of $\pi/2$ can be captured simultaneously by two matched monochrome CCDs (Mintron, MTV-1802CB) with size of 576 (V) × 768 (H) pixels, and the pixel size is 10 μm × 10 μm. In addition, the imaging lens L1 ($f=120$ mm) is employed to project an image of the “prism-droplet” plane onto the CCD with the lateral magnification of 2.5, and another lens L2 with the same L1 parameter is placed in the reference arm to achieve wavefront curvature matching.

Specially, by using our homemade TIR-DCSPSI system, the reflection phase variation of p-polarization can be achieved easily. Actually, the phase calculated from equation (7) contains the reflection phase variation and an additional phase induced by experimental system. If the additional phase is assumed to be constant and unchanged with time, and the air around the prism is uniform with the known refractive index of n_0 . Thus the measured phase distributions $\varphi_{p0}(x, y)$ and $\varphi_{pt}(x, y)$, corresponding to the states without and with the droplet on the prism surface, can be respectively expressed as:

$$\varphi_{p0}(x, y) = \psi_{p0}(x, y) + \varphi_0(x, y) = -2 \arctan \frac{n_1 \sqrt{n_1^2 \sin^2 \theta_1 - n_0^2}}{n_0^2 \cos \theta_1} + \varphi_0(x, y) \quad (10)$$

$$\varphi_{pt}(x, y) = \psi_{pt}(x, y) + \varphi_0(x, y) = -2 \arctan \frac{n_1 \sqrt{n_1^2 \sin^2 \theta_1 - n_2^2(x, y)}}{n_2^2(x, y) \cos \theta_1} + \varphi_0(x, y) \quad (11)$$

where, $\psi_{p0}(x, y)$ and $\psi_{pt}(x, y)$ denote the reflection phase variations induced by “prism-air” and “prism-droplet” interfaces, corresponding to the states without and with the droplet on the prism surface, respectively; $\varphi_0(x, y)$ represents the additional phase induced by the experimental system. By performing the subtraction operation between equations (10) and (11), the additional phase $\varphi_0(x, y)$ can be eliminated. Therefore, the reflection phase variation difference between above two states can be achieved as:

$$\begin{aligned} \Delta \psi_{pt}(x, y) &= \psi_{pt}(x, y) - \psi_{p0}(x, y) = \varphi_{pt}(x, y) - \varphi_{p0}(x, y) \\ &= -2 \arctan \frac{n_1 \sqrt{n_1^2 \sin^2 \theta_1 - n_2^2(x, y)}}{n_2^2(x, y) \cos \theta_1} + 2 \arctan \frac{n_1 \sqrt{n_1^2 \sin^2 \theta_1 - n_0^2}}{n_0^2 \cos \theta_1} \end{aligned} \quad (12)$$

Figure 2(b) illustrates that reflection phase variation differences $\Delta \psi_{pt}$ of different tested samples, i.e. water with $n_2 = 1.3317$ and 80% glycerol-water with $n_2 = 1.4399$, are changed with the incident angle θ_1 in the case that

the $n_1 = 1.5151$ (prism) and $n_0 = 1.0003$ (air)²⁸. It is found that the reflection phase variation difference $\Delta\psi_{pt}$ is reduced with the increasing of the incident angle θ_1 . In the case that $\theta_1 = 72.8^\circ$, the corresponding reflection phase variation difference is enough to ensure the accuracy of the tested droplets.

Thus, the parameters of n_1 , n_0 and θ_1 are known in advance, $\Delta\psi_{pt}(x, y)$ can be determined from equation (12) when the total internal reflection occurs at the “prism-droplet” interface, the corresponding reflection phase variation of p-polarization can be achieved by:

$$\psi_{pt}(x, y) = -2 \arctan \frac{n_1 \sqrt{n_1^2 \sin^2 \theta_1 - n_0^2}}{n_0^2 \cos \theta_1} + \Delta\psi_{pt}(x, y) \quad (13)$$

Deduced from equation (9), the relationship of the refractive indices $n_2(x, y)$, n_1 and the incident angle θ_1 can be expressed as

$$n_2^4(x, y) \cos^2 \theta_1 \tan^2 \left[\frac{\psi_{pt}(x, y)}{2} \right] + n_2^2(x, y) n_1^2 - n_1^4 \sin^2 \theta_1 = 0 \quad (14)$$

Consequently, using the root formula of a quadratic equation, the distribution of a droplet can be calculated by

$$n_2(x, y) = \sqrt{\frac{-n_1^2 + \sqrt{n_1^4 + 4n_1^4 \sin^2 \theta_1 \cos^2 \theta_1 \tan^2 \left[\frac{\psi_{pt}(x, y)}{2} \right]}}{2 \cos^2 \theta_1 \tan^2 \left[\frac{\psi_{pt}(x, y)}{2} \right]}} \quad (15)$$

Results and Discussion

Refractive index distribution of a droplet. To verify the validity of proposed TIR-DCSPSI method, three samples, e.g. deionized water, ethylene glycol and 80% glycerol-water mixture are chosen as the tested objects in an airtight laboratory with temperature of 25 °C and relative humidity of 60%. First, a pair of phase-shifting interferograms with the spatial phase shifts of $\pi/2$ in the case that the sample is not dropped on the prism surface is simultaneously captured by CCD1 and CCD2, respectively. Second, for each tested sample, a pair of phase-shifting interferograms with the spatial phase shifts of $\pi/2$ is captured, as shown in Fig. 4(a1,a2, b1,b2 and c1,c2), in which the size of interferogram is 300(H) × 300(V) pixels and the incident angle of laser beam is 72.8°. Third, by using the spatial carrier-frequency phase-shifting algorithm²⁵ and equation (12), Fig. 4(a3–c3) present the corresponding 2D reflection phase variation difference distributions. It is observed that the reflection phase variation difference distributions in the droplet region are distinctly different from the air background. Based on equations (13) and (15), we achieve the 2D refractive index distributions of deionized water, ethylene glycol and 80% glycerol-water mixture droplets, as shown in Fig. 4(a4–c4), respectively.

Due to various influences, e.g. air flow, mechanical vibration, noise and the different error in different phase revealed by phase-shifting algorithms, there is obvious fluctuation in the 2D reflection phase variation difference distribution as shown in Fig. 4(a3–c3). Meanwhile, the thickness near the droplet edge is very thin, when it reaches the level of evanescent wave range, the reflection phase variation difference distributions (or the refractive index distributions) report on a combination of air and droplet^{17,29}. To address this, we choose a uniform area near the center of the droplet marked as the black rectangles in Fig. 4(a3–c3) to perform calculation. For each kind of droplets, eleven independent measurements are carried out; the average and standard deviation (SD) of multiple measurements are calculated, as shown in Table 1. It is found that the refractive indices, corresponding to water, ethylene glycol and 80% glycerol-water mixture, are 1.3335 ± 0.0013 , 1.4278 ± 0.0001 and 1.4394 ± 0.0001 , respectively. For comparison, these refractive indices were by Abbe refractometer (WAY-2S) and were employed as reference, as shown in Table 1. The root mean square error (RMSE) of the difference between the 2D refractive index distribution achieved with the proposed method and the reference is calculated to indicate the accuracy in 2D space. It is only 0.0009 in measurement of 80% glycerol-water droplet, further indicating that the validity of the proposed method in 2D refractive index distribution measurement.

Dynamic refractive index distribution during a droplet evaporation. Next, by using the proposed method, we perform the dynamic 2D refractive index distribution measurement during a droplet evaporation of sodium carbonate solution. Like the above experimental condition, first, we capture a pair of phase-shifting interferograms with the spatial phase shifts of $\pi/2$ in the case that the sample is not dropped on the prism surface by CCD1 and CCD2, respectively. Second, when a droplet is on the center of the prism surface evaporates, many pairs of interferograms are captured continuously by two CCDs. The capturing rate is 2-frame/second, during a sodium carbonate solution droplet with concentration of 1% (380 seconds) (see Visualization1). Figure 5(a–c) show the 2D refractive index distributions at the time: 0 s, 200 s and 300 s during the droplet evaporation, respectively, in which the size of interferogram is 200(H) × 200(V) pixels. It is observed that the refractive index of the droplet increases with the increasing of evaporation time. Moreover, Fig. 5(d) gives the refractive index distribution variation as function of time at the point marked as P (150, 105) in Fig. 5(a–c), in which the dots represent the measuring values. We can see that the refractive index of the droplet is gradually increased with the time increasing during the first 200 seconds of a droplet evaporation, and then rapidly increased from 200 to 350 seconds. Finally, when the concentration of sodium carbonate solution reaches its saturation value, the corresponding refractive index reaches the maximum value.

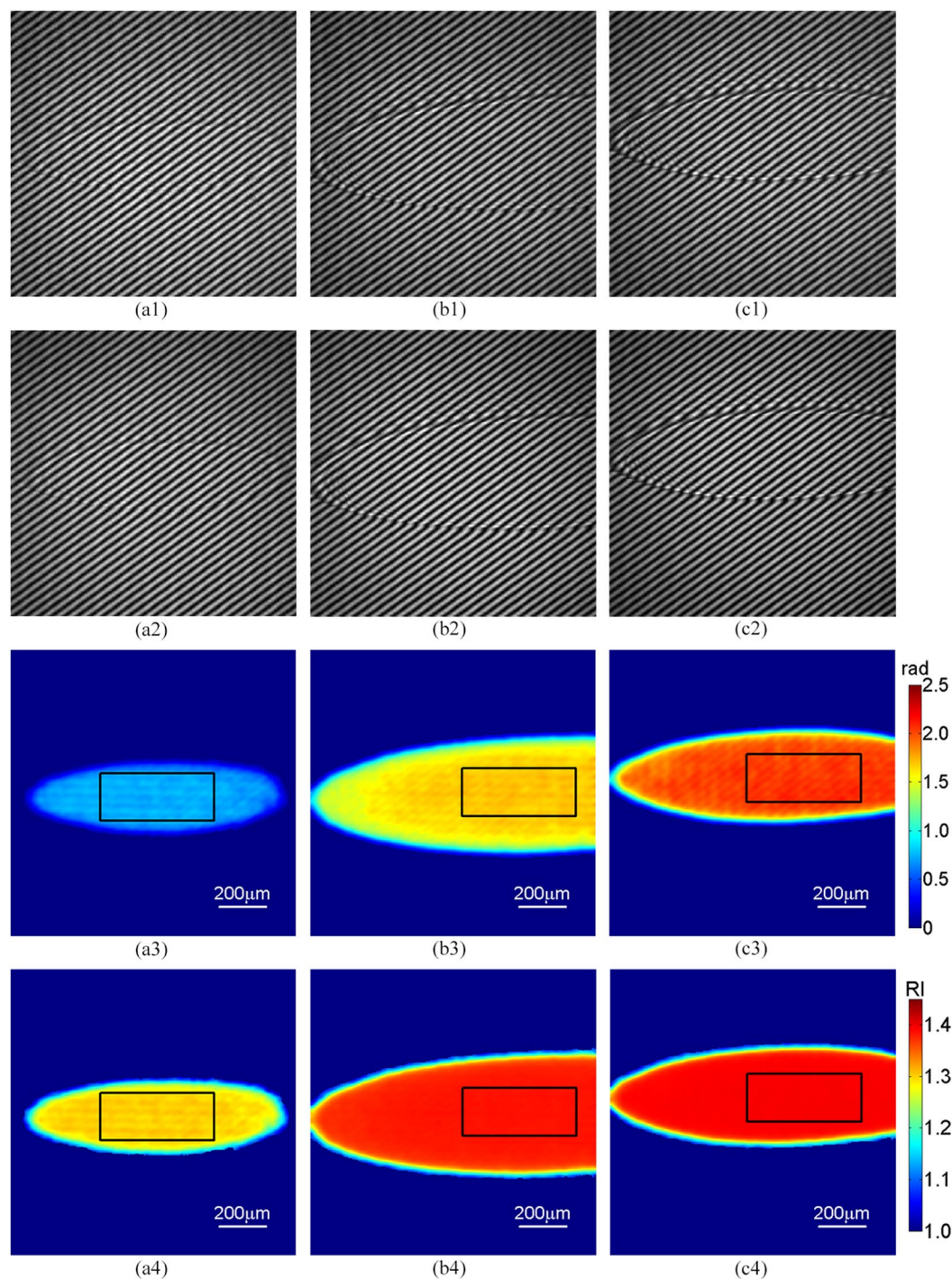


Figure 4. For each droplet, a pair phase-shifting interferograms with the phase shifts of $\pi/2$ are simultaneously captured by two CCDs (a1,a2) deionized water; (b1,b2) ethylene glycol; (c1,c2) 80% glycerol-water mixture; (a3,b3,c3) the corresponding 2D reflection phase variation difference distributions; (a4,b4,c4) the corresponding 2D refractive index distributions.

In contrast, the refractive indices of the sodium carbonate solution droplet with concentration of 1% and 28.4% (corresponding to saturated concentration at 30 °C) measured by Abbe refractometer (WAY-2S) illuminated with 632.8 nm laser are 1.3335 and 1.3979, respectively.

Dynamic refractive index distribution measurement during two droplets mutual solubilization. Next, we try to measure dynamic refractive index distribution during two droplets mutual solubilization through using the proposed TIR-DCPSI method, in which an 80% glycerol-water mixture droplet and a deionized water droplet are chosen as the tested samples in the environment with the temperature of 25 °C and the

Measured sample	Refractive index/RIU (Abbe refractometer)	Refractive index/RIU (TIR-DCSPSI)	SD/RIU (TIR-DCSPSI)	RMSE/RIU (TIR-DCSPSI)
Water	1.3317	1.3335	0.0013	0.0058
40% glycerol-water	1.3810	1.3796	0.0006	0.0025
50% glycerol-water	1.3950	1.3940	0.0005	0.0018
60% glycerol-water	1.4098	1.4089	0.0003	0.0017
70% glycerol-water	1.4246	1.4254	0.0003	0.0014
ethylene glycol	1.4285	1.4278	0.0001	0.0012
80% glycerol-water	1.4399	1.4394	0.0001	0.0009

Table 1. Refractive index measurement results of droplets.

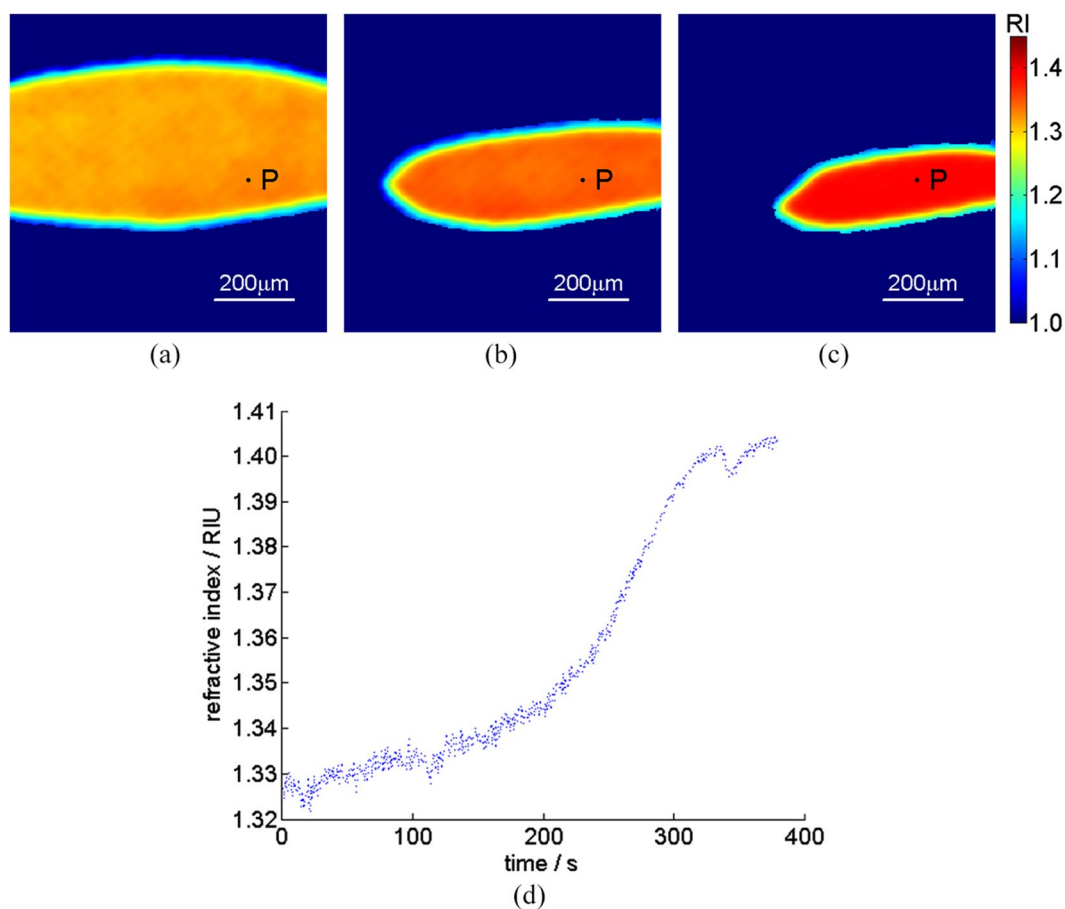


Figure 5. 2D refractive index distribution variation during a droplet evaporation versus the time (see Visualization1) (a) $t = 0$ s; (b) $t = 200$ s; (c) $t = 300$ s; (d) the refractive index distribution variation of the point marked as P in (a–c), respectively.

relative humidity of 60%, the image acquisition speed is set as 20-frames/second and whole mutually soluble process is 100 seconds (see Visualization2), and the size of interferogram is $300(H) \times 250(V)$ pixels. Figure 6(a) shows the 2D refractive index distribution of before two droplets mutual solubilization, set as the initial time point of evaporation. Figure 6(b–d) illustrate the 2D refractive index distribution at the time 0.05 s, 1 s, and 100 s, respectively. It is found that the 2D refractive index distribution is changed during the whole mutual solubilization process until the equilibrium reaches. Figure 6(e) shows the cross-section curves of the lines marked as A (150, 100) and B (150, 200) in (a)–(d), respectively, in which x -axis denotes the pixel position relative to the original point A. We can see that the refractive index of deionized water droplet is different from the glycerol-water mixture droplet before two droplets mutual dissolution, along with two droplets mutual solubilization, the refractive index of mutual dissolution area is gradually changed until the equilibrium reaches. This result further demonstrates the proposed TIR-DCSPSI method is very suitable for the refractive index distribution measurement of dynamic process.

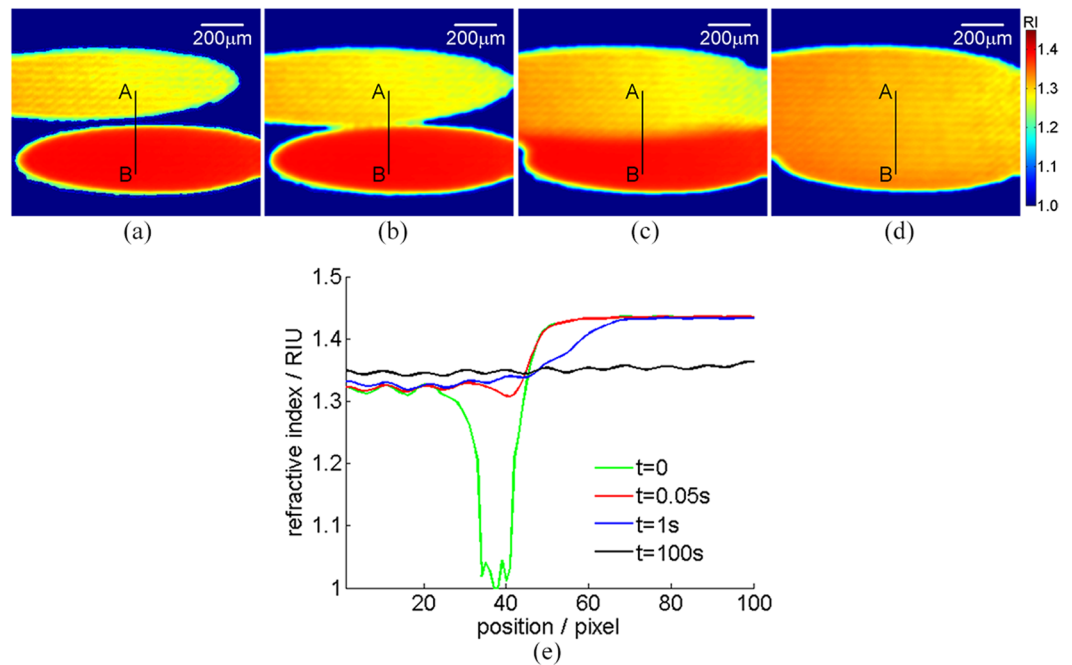


Figure 6. 2D refractive index distribution variation during two droplets mutual solubilization versus the time (see Visualization2) (a) $t = 0$ s; (b) $t = 0.05$ s; (c) $t = 1$ s; (d) $t = 100$ s; (e) the cross-section curves of the lines marked as AB in (a–d), respectively.

Conclusions

In this study, by combining TIR technique and our homemade DCSPSI system, we propose a novel TIR-DCSPSI method to achieve dynamic refractive index distribution during dynamic process. First, a right-angle prism is introduced into the DCSPSI system, the reflection phase variation induced by TIR technique occurring at the “prism-droplet” interface, which contains the refractive index information of tested sample, can be achieved by the spatial carrier-frequency phase-shifting algorithm from a pair of interferograms with the phase shifts of $\pi/2$ captured by DCSPSI system. Second, based on the relationship between the reflection phase variation and the refractive index, the refractive index distribution can be calculated easily. In addition, to improve the measuring accuracy and reduce the error induced by noise, we choose the orthogonal polarization interferometry system to make full use of the light energy, and the p-polarization of TIR as the object beam. Importantly, the proposed TIR-DCSPSI method will supply a useful tool for dynamic refractive index distribution measurement of dynamic process, such as the droplet evaporation, mutual solubilization of different droplets, diffusion, cell culture, colloid curing and other fields.

References

1. Volkmann, H. Ernst Abbe and his work. *Appl. Optics*. **5**, 1720–1731 (1966).
2. Axelrod, D. Cell-substrate contacts illuminated by total internal reflection fluorescence. *J. Cell Biol.* **89**, 141–145 (1981).
3. Axelrod, D., Thompson, N. L. & Burghardt, T. P. Total internal reflection fluorescent microscopy. *J. Microsc.* **129**, 19–28 (1983).
4. Patskovsky, S., Meunier, M. & Kabashin, A. V. Phase-sensitive silicon-based total internal reflection sensor. *Opt. Express*. **15**, 12523–12528 (2007).
5. Zhu, X. *et al.* Ultrasonic detection based on polarization dependent optical reflection. *Opt. Lett.* **42**, 439–441 (2017).
6. Calabuig, A., Matrecano, M., Paturzo, M. & Ferraro, P. Common-path configuration in total internal reflection digital holography microscopy. *Opt. Lett.* **39**, 2471–2474 (2014).
7. Goyal, K. G. *et al.* Empirical model of total internal reflection from highly turbid media. *Opt. Lett.* **38**, 4888–4891 (2013).
8. Sun, T. *et al.* Measurement of complex refractive index of turbid media by scanning focused refractive index. *Opt. Lett.* **41**, 3767–3770 (2016).
9. Calhoun, W. R., Maeta, H., Combs, A., Bali, L. M. & Bali, S. Measurement of the refractive index of highly turbid media. *Opt. Lett.* **35**, 1224–1226 (2010).
10. Gissibl, T., Wanger, S., Sykora, J., Schmid, M. & Giessen, H. Refractive index measurements of photoresists for three-dimensional direct laser writing. *Opt. Mater. Express*. **7**, 2293–2298 (2017).
11. Chiu, M., Lee, J. & Su, D. Refractive-index measurement based on the effects of total internal reflection and the uses of heterodyne interferometry. *Appl. Optics*. **36**, 2936–2939 (1997).
12. Chiu, M., Lee, J. & Su, D. Complex refractive-index measurement based on Fresnel’s equations and the uses of heterodyne interferometry. *Appl. Optics*. **38**, 4047–4052 (1999).
13. Horst, S. & John, H. B. In *Optical Shop Testing, Third Edition*, (Malacara, D.) 547–655 (John Wiley & Sons, 2006).
14. Yamaguchi, I. & Zhang, T. Phase-shifting digital holography. *Opt. Lett.* **22**, 1268–1270 (1997).
15. Awatsuji, Y., Sasada, M. & Kubota, T. Parallel quasi-phase-shifting digital holography. *Appl. Phys. Lett.* **85**, 1069–1071 (2004).
16. Shaked, N. T., Rinehart, M. T. & Wax, A. Dual-interference-channel quantitative-phase microscopy of live cell dynamics. *Opt. Lett.* **34**, 767–769 (2009).
17. Ash, W. M. & Kim, M. K. Digital holography of total internal reflection. *Opt. Express*. **16**, 9811–9820 (2008).

18. Jian, Z., Hsieh, P., Hsieh, H., Chen, H. & Su, D. A method for measuring two-dimensional refractive index distribution with the total internal reflection of p-polarized light and the phase-shifting interferometry. *Opt. Commun.* **268**, 23–26 (2006).
19. Kreis, T. Digital holographic interference-phase measurement using the Fourier-transform method. *J. Opt. Soc. Am. A* **3**, 847–855 (1986).
20. Smythe, R. & Moore, R. Instantaneous phase measuring interferometry. *Opt. Eng.* **23**, 361–364 (1984).
21. Kwon, O. Y. Multichannel phase-shifted interferometer. *Opt. Lett.* **9**, 59–61 (1984).
22. Hettwer, A., Kranz, J. & Schwider, J. Three channel phase-shifting interferometer using polarization-optics and a diffraction grating. *Opt. Eng.* **39**, 960–966 (2000).
23. Jiao, S. & Zou, W. High-resolution parallel phase-shifting digital holography using a low-resolution phase-shifting array device based on image inpainting. *Opt. Lett.* **42**, 482–485 (2017).
24. Sun, P., Zhong, L., Luo, C., Niu, W. & Lu, X. Visual measurement of the evaporation process of a sessile droplet by dual-channel simultaneous phase-shifting interferometry. *Sci. Rep.-uk.* **5**, 12053 (2015).
25. Qiu, X. *et al.* A rapid spatial carrier-frequency phase-shifting method based on the orthogonality of diamond diagonal vectors. *IEEE Photonics J.* **9**, 6900409, <https://doi.org/10.1109/JPHOT.2017.2697042> (2017).
26. Born, M. & Wolf, E. In *Principles of Optics, seventh Edition* (Born, M. & Wolf, E.) 38–54 (Cambridge, 2005).
27. Snyder, A. W. & Love, J. D. Goos-Hanchen shift. *Appl. Optics.* **15**, 236–238 (1976).
28. Ciddor, P. E. Refractive index of air: new equations for the visible and near infrared. *Appl. Optics.* **35**, 1566–1573 (1996).
29. Yeh, P. In *Optical Waves in Layered Media, First Edition*, (Yeh, P.) 86–87 (John Wiley & Sons, 1988).

Acknowledgements

This work is supported by National Nature Science Foundation of China grants (61475048, 61727814, and 61575069).

Author Contributions

X.L., L.Z. and Y.Z. conceived and designed the idea, Y.Z. performed the experiments, X.L., L.Z. and Y.Z. analyzed the experiments data, X.L., L.Z., Y.Z., H.Z., J.L., B.L. and J.T. wrote the paper. All authors helped with manuscript preparation and revision.

Additional Information

Supplementary information accompanies this paper at <https://doi.org/10.1038/s41598-018-33299-w>.

Competing Interests: The authors declare no competing interests.

Publisher's note: Springer Nature remains neutral with regard to jurisdictional claims in published maps and institutional affiliations.



Open Access This article is licensed under a Creative Commons Attribution 4.0 International License, which permits use, sharing, adaptation, distribution and reproduction in any medium or format, as long as you give appropriate credit to the original author(s) and the source, provide a link to the Creative Commons license, and indicate if changes were made. The images or other third party material in this article are included in the article's Creative Commons license, unless indicated otherwise in a credit line to the material. If material is not included in the article's Creative Commons license and your intended use is not permitted by statutory regulation or exceeds the permitted use, you will need to obtain permission directly from the copyright holder. To view a copy of this license, visit <http://creativecommons.org/licenses/by/4.0/>.

© The Author(s) 2018